

FRONTIER ARTICLE

10.1002/2015GL063946

Key Points:

- Time domain structures produce field-aligned electron pitch angle distributions
- Field-aligned electrons are seeds for relativistic electron acceleration
- TDS cause electron precipitation that produces some types of auroras

Correspondence to:

F. S. Mozer,
forrest.mozer@gmail.com

Citation:

Mozer, F. S., O. V. Agapitov, A. Artemyev, J. F. Drake, V. Krasnoselskikh, S. Lejosne, and I. Vasko (2015), Time domain structures: What and where they are, what they do, and how they are made, *Geophys. Res. Lett.*, 42, 3627–3638, doi:10.1002/2015GL063946.

Received 22 MAR 2015

Accepted 28 APR 2015

Accepted article online 29 APR 2015

Published online 29 MAY 2015

Time domain structures: What and where they are, what they do, and how they are made

F. S. Mozer¹, O. V. Agapitov^{1,2}, A. Artemyev³, J. F. Drake⁴, V. Krasnoselskikh⁵, S. Lejosne¹, and I. Vasko³

¹Space Sciences Laboratory, University of California, Berkeley, California, USA, ²Taras Shevchenko National University of Kiev, Kiev, Ukraine, ³Space Research Institute, Russian Academy of Science, Moscow, Russia, ⁴Physics Department, University of Maryland, College Park, Maryland, USA, ⁵LPC2E/CNRS-University of Orleans, Orleans, France

Abstract Time domain structures (TDS) (electrostatic or electromagnetic electron holes, solitary waves, double layers, etc.) are ≥ 1 ms pulses having significant parallel (to the background magnetic field) electric fields. They are abundant through space and occur in packets of hundreds in the outer Van Allen radiation belts where they produce magnetic-field-aligned electron pitch angle distributions at energies up to a hundred keV. TDS can provide the seed electrons that are later accelerated to relativistic energies by whistlers and they also produce field-aligned electrons that may be responsible for some types of auroras. These field-aligned electron distributions result from at least three processes. The first process is parallel acceleration by Landau trapping in the TDS parallel electric field. The second process is Fermi acceleration due to reflection of electrons by the TDS. The third process is an effective and rapid pitch angle scattering resulting from electron interactions with the perpendicular and parallel electric and magnetic fields of many TDS. TDS are created by current-driven and beam-related instabilities and by whistler-related processes such as parametric decay of whistlers and nonlinear evolution from oblique whistlers. New results on the temporal relationship of TDS and particle injections, types of field-aligned electron pitch angle distributions produced by TDS, the mechanisms for generation of field-aligned distributions by TDS, the maximum energies of field-aligned electrons created by TDS in the absence of whistler mode waves, TDS generation by oblique whistlers and three-wave-parametric decay, and the correlation between TDS and auroral particle precipitation, are presented.

1. Introduction

The name “time domain structures” (TDS) was initially given to packets of ≥ 1 ms duration intense electric field spikes detected by the Van Allen Probes in the Earth’s outer radiation belts. These electric field spikes had significant components parallel to the local magnetic field and each packet contained as many as hundreds of such spikes [Mozer *et al.*, 2013]. The velocity of propagation of these TDS along magnetic field lines was found to be close to the thermal speed of 100–200 eV electrons, and they were identified as electron acoustic-like perturbations of the plasma density and electric field. Van Allen Probe observations have shown that at least five different types of intense electric field spikes exist and they were united by the common title “TDS.” These types include electrostatic and electromagnetic double layers, electrostatic and electromagnetic electron holes, and nonlinear whistlers, all of which were known and studied earlier. Because these TDS are abundant in the observations, it has been suggested that they are an important factor in the macroscopic dynamics of the radiation belts, providing the mechanism of acceleration of low-energy electrons up to keV energies after which they are further acceleration by whistler waves to relativistic energies in the radiation belts [Mozer *et al.*, 2014]. They may also be responsible for producing field-aligned electron fluxes that make auroras.

2. Types of TDS

Figure 1 illustrates examples of different types of TDS found on the Van Allen Probes in the Earth’s outer radiation belt by the Electric Fields and Waves (EFW) [Wygant *et al.*, 2013] and Electric and Magnetic Field Instrument Suite and Integrated Science (EMFISIS) [Kletzing *et al.*, 2013] instruments. In each of the four sections of this figure, Figures 1a–1c give the electric field perturbations in magnetic-field-aligned coordinates and Figures 1e–1f give the magnetic field perturbations in the same frame, with the parallel components located in Figures 1c and 1f of each section. Observationally, it is not clear which, if any, of

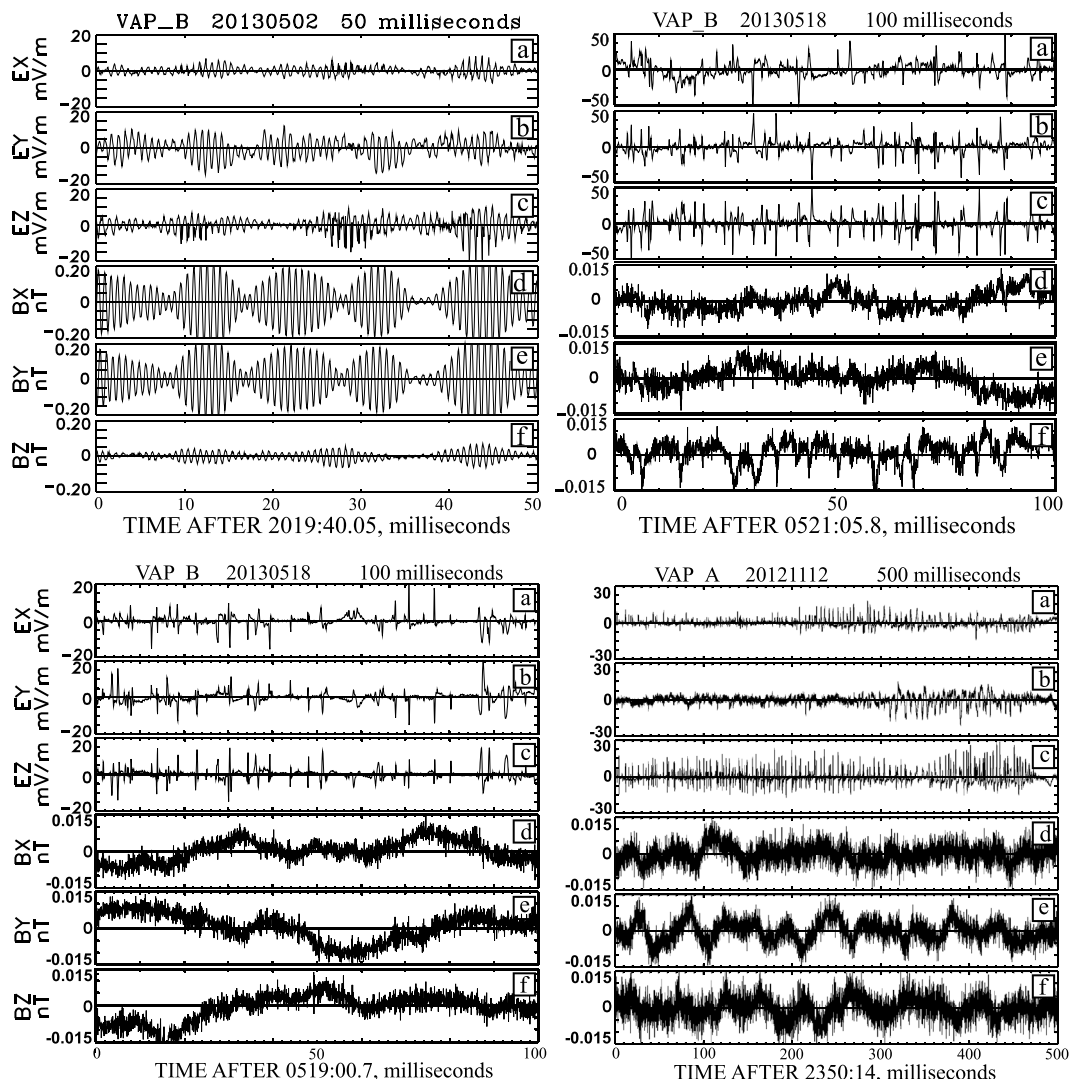


Figure 1. Examples of different types of time domain structures found by the Van Allen Probes. (top left) A nonlinear whistler whose parallel electric field is distorted by electron trapping that produces spin-periodic unidirectional spikes [Kellogg *et al.*, 2010]. (bottom left) Structures that are called electrostatic electron holes because the parallel electric field signature is largely bipolar, and there is no comparable magnetic field signature. (top right) Electron holes that are magnetized because the electric field spikes are frequently accompanied by structures in the parallel magnetic field component [Andersson *et al.*, 2009; Tao *et al.*, 2011; Vasko *et al.*, 2015]. (bottom right) Bipolar electron holes that evolve into single-sided electric field structures called double layers.

these structures contain a net parallel electric potential. It is noted that whistlers were present in only one of the four examples (Figure 1, top left), which is typical of the overall data observed in the Van Allen radiation belts. Instead, in each of the three other sections, there is low-frequency (a few tens of hertz) noise in the magnetic field, which may result from Doppler shifted kinetic Alfvén waves [Chaston *et al.*, 2014]. This low-frequency magnetic noise is typical of TDS observations in the radiation belts. It is also noted that the TDS in this figure are three-dimensional objects because they produce spiky signatures in the perpendicular as well as the parallel electric field.

3. TDS Appearance Following Plasma Injections

Figure 2 presents an example of a plasma injection into the outer radiation belt followed, a few minutes later, by electromagnetic energy injection, TDS, and electrons that were field-aligned to energies of 100 keV. In this and all examples discussed in this paper, events were selected on the basis of the presence of TDS in the

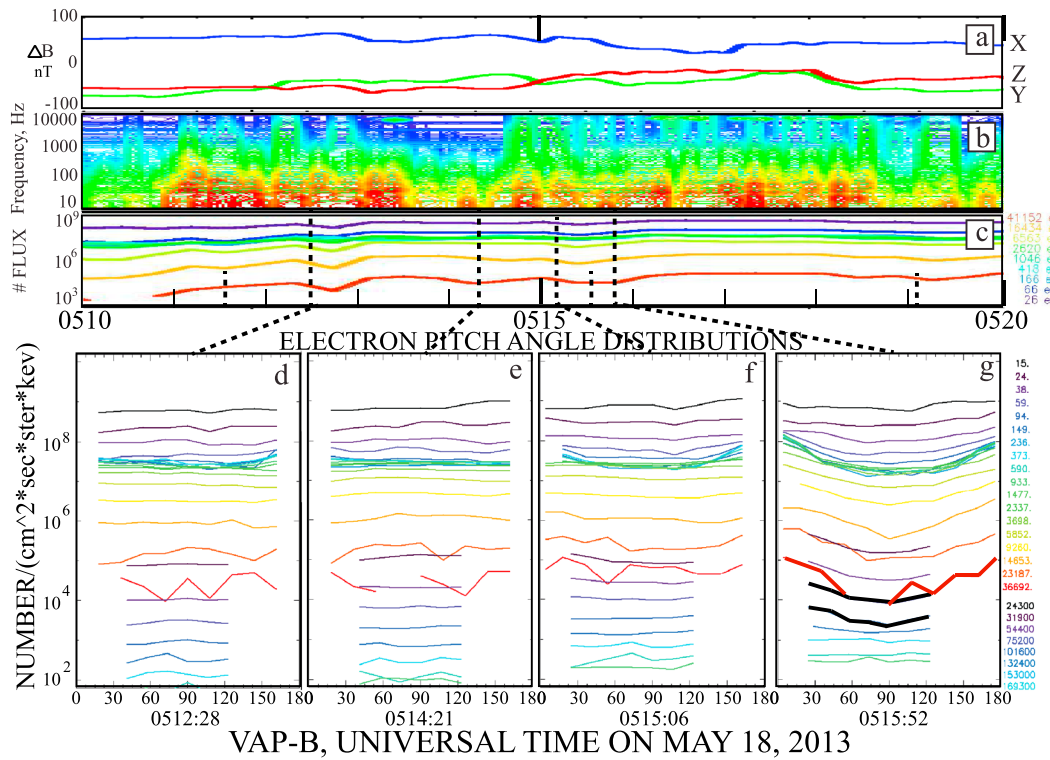


Figure 2. Fields and plasma measured at a magnetic local time of 2210, magnetic latitude of 14.5° , and an L value of 5.9. In Figure 2a, the X component is black, the Y component is green, and the Z component is red. The remaining quantities are defined and described in the main text. The energy units at the rights of the plots are eV.

absence of whistlers, in order to study the effects caused by TDS alone. Figure 2a presents the three components of $\Delta B = (B_{\text{measured}} - B_{\text{model}})$ in GSE coordinates during the 10 min interval covered in the figure, where B_{model} is obtained from a Tsyganenko [1995]. Figure 2b gives the electric field frequency spectrum, and Figure 2c gives nine Helium, Oxygen, Proton, Electron plasma spectrometer (HOPE) detector electron number fluxes from 26 eV to 41 keV [Spence *et al.*, 2013]. Figures 2d through 2g provide pitch angle distributions of the HOPE-detected and Magnetic Electron Ion Spectrometer (MagEIS)-detected electrons at the 4 times illustrated by the long, vertical, dashed lines in Figure 2c. These data were collected at a 20 s cadence. Shortly after 0510 UT, the electron fluxes in Figure 2c increased at all energies due to the injection of electrons from further down the tail. At this time, the low-frequency electric field amplitude of Figure 2b increased due to electromagnetic noise that was also observed in the magnetic field (not shown) and in a burst of high time resolution electric and magnetic field waveforms (not shown) at about 0511:20, the time of the first short vertical dashed line in Figure 2c. The electron pitch angle distribution of Figure 2d, obtained during the flux increase, at the position of the first long vertical dashed line in Figure 2c, showed that electrons of all energies were approximately isotropic during the injection. After the injection was complete, at 0514:21, the pitch angle distribution of Figure 2e remained isotropic and the electrons were apparently not influenced by the low-frequency noise. Forty seconds later, ΔB_Z (the red curve in Figure 2a) indicated a current associated with dipolarization of the magnetic field. Along with this current, the pitch angle distribution of Figure 2f began to show field-aligned distributions of 0.1–1 keV electrons (the green curves) at the same time that TDS, intermixed with the low-frequency noise, first appeared (not shown). During the next 45 s, the TDS intensity increased and the pitch angle distributions became magnetic field aligned at all energies from 0.1 to 100 keV in Figure 2g. At energies of 20–50 keV, the HOPE and MagEIS data overlap with the HOPE data covering a wider pitch angle range and MagEIS providing better counting statistics. The thick red curve in Figure 2g gives the HOPE pitch angle distribution at 37 keV, and the two thick black curves give the MagEIS distributions at 55 and 75 keV. Thus, both the HOPE and the MagEIS data are required to

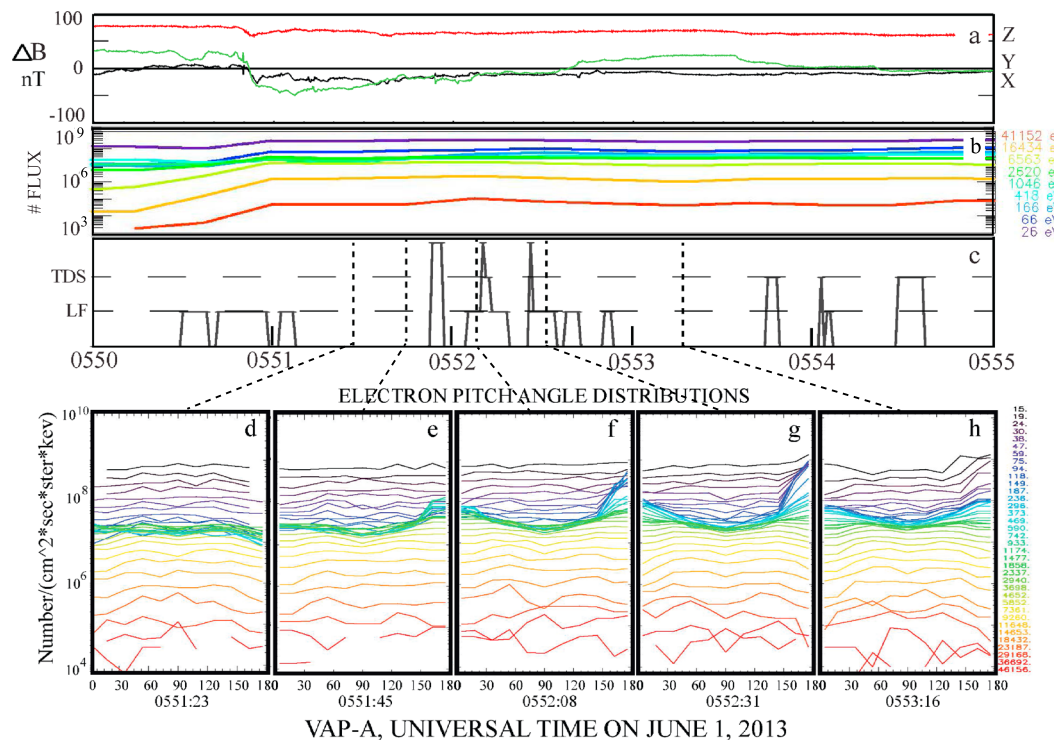


Figure 3. Fields and plasma measured at a magnetic local time of 2310, magnetic latitude of 18.7°, and an L value of 11. In Figure 3a, the X component is black, the Y component is green, and the Z component is red. The remaining quantities are defined and described in the main text.

make the case that the electrons were field aligned to energies as high as 100 keV. It is noted that the field-aligned electron flux exceeded the 90° flux by an order of magnitude at most energies. Examples of the TDS observed shortly after this interval are given in Figure 1 (bottom left) (electrostatic electron holes with amplitudes ~ 15 mV/m) and Figure 1 (top right) (electromagnetic electron holes with amplitudes ~ 50 mV/m).

A second example of the same temporal behavior of plasma injection followed a few minutes later by TDS and pitch angle deformation is given in Figure 3. Figure 3a gives ΔB during a 5 minute interval and Figure 3b gives nine HOPE electron fluxes from 26 eV to 41 keV. Because there were many short duration bursts of high time resolution data collected during this time, a summary of the bursts rather than the spectrum of the electric field signal is given in Figure 3c. At times when the curve of Figure 3c is at the lower level (labeled LF), low-frequency noise was detected in the time domain bursts of wave data. (While the low-frequency noise is not relevant to the present paper, its presence is included for completeness.) When the curve is at the middle level (labeled TDS), TDS alone were observed and when the curve is at the top of the panel, both TDS and low-frequency noise were observed. These TDS were three-dimensional electromagnetic holes, similar to the example in Figure 1 (top right). This is determined by the presence of the perpendicular electric field components in the TDS that were comparable with the parallel components and the presence of parallel magnetic fields that in these TDS were significant. The electric field amplitudes varied between about 15 and 40 mV/m. Between 0550 and 0551 UT, injected electrons appeared at the spacecraft with low-frequency noise and no TDS. At 0551:23 (the time of the first vertical dashed line in Figure 3c), Figure 3d shows that the pitch angle distributions resulting from the injection were peaked at 90°. By 0551:45 (the second vertical dashed line in Figure 3c), 20 s later, the pitch angle distribution of 0.1–1 keV electrons started to have a peak at a pitch angle of 180°, as seen in Figure 3e. Just before 0552 and throughout the remaining interval, TDS, sometimes with low-frequency noise, were observed, while the pitch angle distributions of Figure 2f, and 2g, showed an increasing anisotropy with the flux at 180° of 100 eV to 1 keV electrons exceeding that at smaller angles by an order of magnitude. This flux constituted a beam in the given energy range. Thus, in this example also, the plasma injection preceded the TDS and field-aligned electron distribution by about 1 min.

4. TDS Theories and Observations

As a plasma physics process, electron hole TDS were first studied in numerical models of the instability of two electron beams [Roberts and Berk, 1967; Morse and Nielson, 1969a, 1969b]. Their generation was first observed in the lab in a Q-machine by Saeki *et al.* [1979]. Generation by spontaneous reconnection in a toroidal device was studied [Fox *et al.*, 2008], and laboratory observations of electron holes in a plasma device have been presented [Lefebvre *et al.*, 2011].

Double layer-type TDS were first discussed in connection with magnetospheric physics and astrophysics by the Stockholm group under Hannes Alfvén [Alfvén and Carlqvist, 1978, and references therein; Raadu, 1989]. TDS were first observed in the magnetosphere along auroral zone magnetic field lines on the S3-3 satellite [Mozer *et al.*, 1977; Temerin *et al.*, 1982] and they were more thoroughly studied on the FAST mission [Ergun *et al.*, 1998, 2001]. They have been seen in the tail [Matsumoto *et al.*, 1994; Franz *et al.*, 1998; Streed *et al.*, 2001], the plasma sheet [Ergun *et al.*, 2009; Deng *et al.*, 2010], the plasma sheet boundary layer [Lakhina *et al.*, 2010], at shocks [Bale *et al.*, 1998; Cattell *et al.*, 2003], at magnetic field reconnection sites [Cattell *et al.*, 2002; Mozer and Pritchett, 2009a, 2009b; Khotyaintsev *et al.*, 2010; Li *et al.*, 2014], in the solar wind [Bale *et al.*, 1996; Malaspina *et al.*, 2013; Williams *et al.*, 2005], and at Saturn [Williams *et al.*, 2006]. However, the huge numbers of TDS in a single event [Mozer *et al.*, 2013] and the large occurrence frequency of such events [Malaspina *et al.*, 2014] were very new and unusual statistical properties of TDS. In the radiation belts they are often the major and dominant element of the wave activity. This raised an important question on their role in processes of particle acceleration and losses. Indeed, it was shown that they play an important role in providing seed electrons that are further accelerated by whistler waves to relativistic energies in the outer radiation belts. This was described and unambiguously evidenced by Mozer *et al.* [2014]. They also are a possible mechanism for precipitating electrons that may be important for certain types of auroras.

5. TDS and Auroral Particle Precipitation

Because, as shown, TDS produce field-aligned electrons that can be lost in several bounces, it is interesting to correlate such events with auroral emissions measured in the Canadian and Alaskan all-sky camera network [Donovan *et al.*, 2006; Mende *et al.*, 2008] in order to understand the role of TDS in producing auroras. The ratio between the HOPE electron flux near the loss cone (the average of the 18, 36, 144, and 162° fluxes) and the 90° flux was computed (as shown for one case in Figure 4b) to identify time intervals of field-aligned electron distributions and possible precipitation. Of 81 events during which a Van Allen Probe was in conjunction with an all-sky imager recording auroral activity, five cases presented concurrent variations of wave activity, pitch angle ratios greater than one, and variations of the light intensity around the conjugate footprint. TDS were present in all five cases and no other wave modes were present at times of auroral precipitation in any of the five events. The event on 26 April 2013, when Van Allen Probe A was in magnetic conjunction with the all-sky imager at Le Pas, Canada, is presented in Figure 4. Because the mapping of the spacecraft footprint is not precise, primarily in the latitudinal direction, the white light intensity averaged over a $\pm 1^\circ$ latitude window around the footprint location was computed, as shown in Figure 4a. Because of moonlight, the background light intensity measured by the all-sky imager was not spatially uniform. To correct for this, the 1 h averaged light background was subtracted from each individual measurement. Clouds were present around the spacecraft footprint at the two time intervals, from 06:15 to 06:30 and from 06:58 to 07:03; these time intervals are reported in blue along the abscissa of Figure 4a. Figure 4b gives the ratios of the field aligned to 90° electron flux for five energy ranges centered at 300 eV, 1 keV, 3 keV, 10 keV, and 30 keV. A ratio of one indicates an isotropic pitch angle distribution while a ratio greater than one indicates a predominately field-aligned pitch angle distribution. Figure 4c gives the amplitude of the electric field spectra at about 75 Hz, which is the broad-band electrostatic noise (BEN) indicator of the presence of TDS, and Figure 4d gives the amplitude of the electric field spectra in the chorus frequency range. The presence of TDS was confirmed in the high time resolution waveform data bursts that occurred several times during the interval of interest. The TDS occurrence rate (Figure 4c) increased as the ratio between field-aligned and equatorial particles increased for all five energy ranges (Figure 4b) while auroral emission appeared (Figure 4a). Thus, this example suggests that TDS produced the field-aligned pitch angle distributions that filled the loss cone with electrons of energy such that

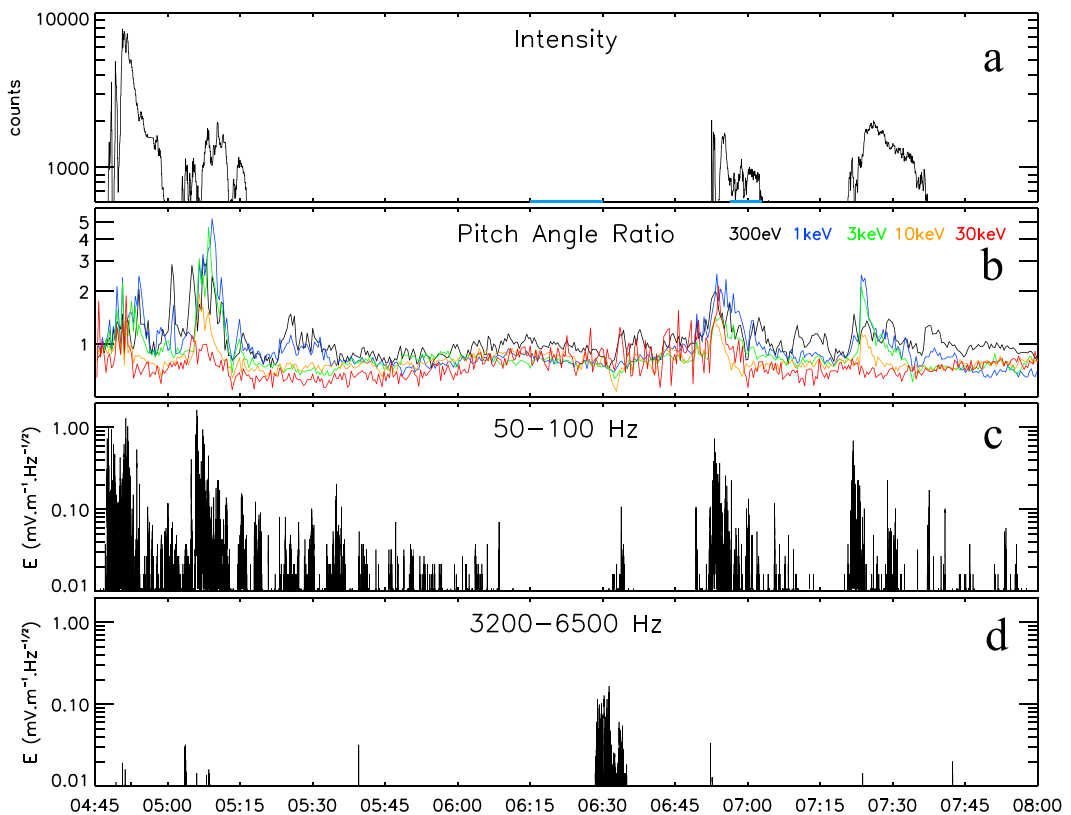


Figure 4. Correlation between Van Allen Probe A electric fields and plasma with auroral light intensity observed at Le Pas, Canada, on 26 April 2013.

auroral light was emitted. It is noted that the electric field wave power due to TDS exceeded the wave power in the chorus range by a factor greater than 10,000 during the correlated time intervals, and the one burst of chorus emission (Figure 4d at 0630) did not produce field-aligned electrons or bright auroral light.

6. TDS Generation in a Particle-In-Cell Simulation

TDS generation from whistlers [Karpman and Kaufman, 1982; Shapiro and Ride, 1994; Kellogg et al., 2010; Agapitov et al., 2014] and by electric currents or beams [Roberts and Berk, 1967; Morse and Nielson, 1969a, 1969b; Lashmore-Davies and Martin, 1973; Joyce and Hubbard, 1978; Hubbard and Joyce, 1979; Yamamoto and Kan, 1985; Omura et al., 1996, 2008; Berthomier et al., 1998; Miyake et al., 1998; Goldman et al., 1999; Newman et al., 2001; Oppenheim et al., 2001; Singh, 2003; Wu et al., 2011] have been studied theoretically. Earlier work [Roth et al., 1999], more recent work [Artemyev et al., 2012, 2013, 2014a; Artemyev, 2014; Osmane and Hamza, 2012a, 2012b], and recent particle-in-cell simulations [Drake et al., 2015] illuminate the relationship between oblique whistlers and TDS generation. The simulation that is illustrated in Figure 5 [Drake et al., 2015], was initialized by a temperature anisotropy in the center of the simulation box that is to the right of the data shown. Thus, the waves and TDS move to the left in Figures 5a and 5b. The fronts of the perpendicular whistler magnetic field at a fixed time are illustrated in Figure 5a. At the same time, the parallel electric field is plotted across the box in Figure 4b with the lighter regions indicating the locations of large parallel electric fields in the TDS. The signals as a function of time (the vertical axis) are given of the perpendicular magnetic field (Figure 5c) and parallel electric field (Figure 5d), as measured along the dashed lines in Figures 5a and 5b. From these data it is clear that the TDS parallel electric field spikes moved at the phase velocity of the whistler. The red regions in Figures 5a and 5b cover locations where the wave normal angle (the angle between its k -vector and the background magnetic field) was greater than 15°; i.e., regions where the wave was oblique. It is seen that the TDS of panel 5b were made in these red locations where the whistler was oblique. Field-aligned electron beams, produced as whistlers

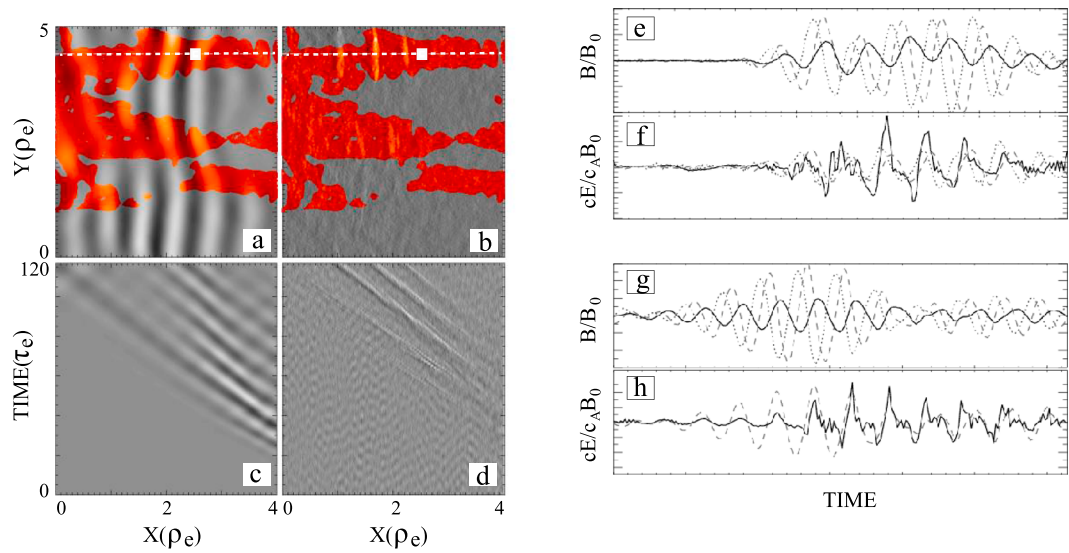


Figure 5. Electric and magnetic fields observed in a particle-in-cell simulation in which oblique whistlers produced time domain structures. (a and b) The perpendicular magnetic field and parallel electric field inside a region of the box that is to the left of the source. (c and d) The position as a function of time (the vertical axis) of the perpendicular magnetic field and parallel electric field, from which it is seen that both parameters move together at the same speed. (e and f) The simulation magnetic and electric fields at a fixed point as a function of time. (g and h) The same quantities, as measured in space.

grew because of the initial electron temperature anisotropy, amplify the parallel electric field of the oblique whistler to produce the TDS structures [Drake *et al.*, 2015]. Figure 5e gives the wave perpendicular magnetic field, and Figure 5f gives the parallel electric field from the simulation as functions of time at the location of the small white boxes in Figures 5a and 5b. Figures 5g and 5h provide an example of the same measured quantities on the Van Allen Probes. The striking similarity of the TDS waveforms in experiment and simulation provide further evidence that one generation mechanism for TDS in the outer radiation belt is from oblique whistlers. The comparison of the simulation and measured electric fields is further discussed in Drake *et al.* [2015].

7. TDS Generation by a Parametric Instability

Another TDS generation mechanism observed in space and modeled analytically is TDS formation from a parametric instability in which a whistler at frequency ω_0 and \mathbf{k} -vector \mathbf{k}_0 decays into a second whistler at ω_1 , \mathbf{k}_1 , and an electron acoustic wave at ω_2 , \mathbf{k}_2 , with $\omega_0 = (\omega_1 + \omega_2)$ and $\mathbf{k}_0 = (\mathbf{k}_1 + \mathbf{k}_2)$. It is worth noting that these whistler waves are in the chorus frequency range, the higher frequency in the upper band, and the lower frequency in the lower band whistlers. Because the two whistlers travel in opposite directions, the magnitude of \mathbf{k}_2 is the sum of the magnitudes of \mathbf{k}_0 and \mathbf{k}_1 , so the low-frequency, $(\omega_0 - \omega_1)$, wave has a very short wavelength and is an electron acoustic signal that quickly evolves into TDS. The possibility of the decay of a whistler wave into an electron acoustic wave that decays into TDS has not been considered before because of the supposed, but incorrect, large linear damping rate of the electron acoustic wave. Figure 6 illustrates this parametric instability in experimental data collected on the Van Allen Probes. Figure 6a presents the perpendicular magnetic field over a 0.5 s time interval and Figure 6b gives the parallel electric field during the same interval. The low-frequency beats of the envelope in Figure 6a result from the presence of two whistlers with slightly different frequencies, and the spikes in Figures 6b signify the presence of large numbers of TDS. The black curve of Figure 6c is the spectrum of the magnetic field, which was composed of two nearly monochromatic waves at frequencies labeled f_0 and f_1 . The blue and red bars in Figure 6c (bottom) indicate the direction of $(\mathbf{E} \times \mathbf{B})/B^2$, which shows that the two waves traveled in opposite directions, as required for the parametric instability. The red curve of Figure 6c is the spectrum of the parallel electric field TDS. This spectrum peaked at $(f_0 - f_1)$ as is required by the instability, but it spread into harmonics as the electron acoustic wave decayed into the observed TDS. Thus, Figure 6 illustrates another way that TDS can be formed from whistlers. (It is noted that most of the TDS in the 200

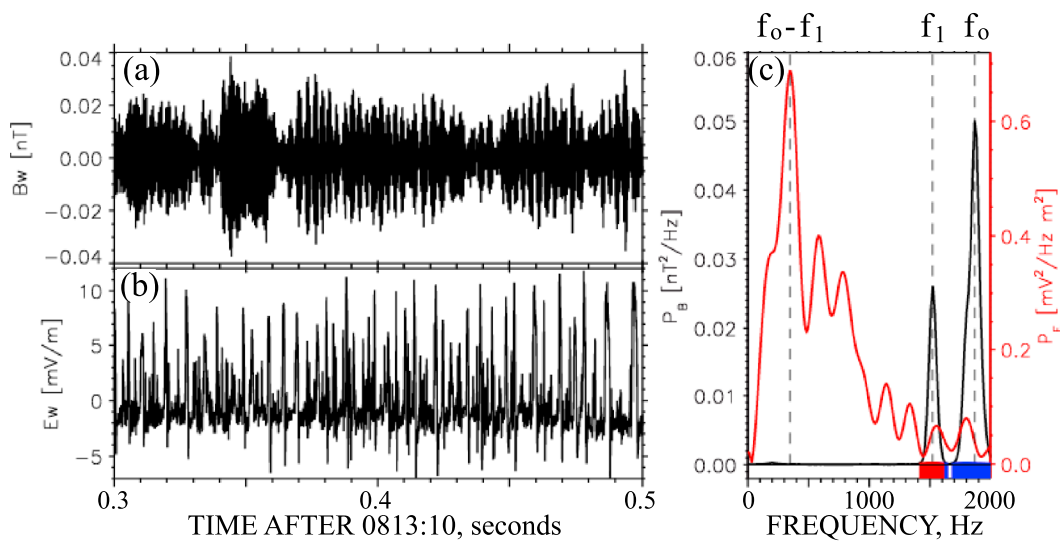


Figure 6. Electric and magnetic fields observed in space during the parametric instability of a whistler wave into a second whistler and an electron acoustic wave that decays into TDS.

examples surveyed in this paper were probably generated by currents or beams because none of them were observed in the presence of whistlers).

8. Statistics of Field-Aligned Electron Distributions

During the first 11 months of Van Allen Probe operations, 200 events on the nightside having TDS in the absence of chorus frequency range whistlers were studied in order to determine the effects of TDS alone. (The absence of whistlers was determined by the electric and magnetic field spectra not having energy in the range of 3200–6500 Hz.) Their typical durations, as judged by low-frequency broad band noise in the electric field spectra in the absence of whistlers, ranged from a few minutes to a few hours. For each TDS event, the maximum field-aligned energy was estimated within an uncertainty of about 50%. These results produced the bar chart of Figure 7, which has an energy resolution of a factor of three. Field-aligned distributions having maximum energies from a few tens of eV to 100 keV were found, with the average energy being 7.6 keV and the number of events having field-aligned distributions at energies greater than

30 keV being about 10% of the total. A most significant result is that all of the selected 200 events having TDS also contained field-aligned electron distributions at times. This is strong evidence that the parallel electric fields in the TDS and the field-aligned electron pitch angle distributions are related. (Field-aligned electrons were observed previously [Abel *et al.*, 2002a, 2002b] and no statistical evidence of a correlation between such electrons and chorus or electron cyclotron harmonic waves was found).

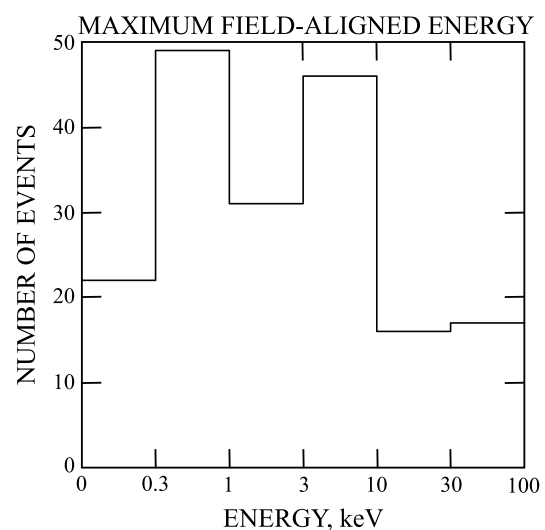


Figure 7. The distribution of the maximum field-aligned electron energies observed in 200 TDS events without whistlers.

9. Discussion

Figures 2 and 3 illustrate two examples in which plasma injected from further down the tail to the satellite location had initial pitch angle distributions that were isotropic or peaked at 90°. Following these injections by a few minutes, TDS and field-aligned electrons appeared together and, in one of the two cases, at the time of a

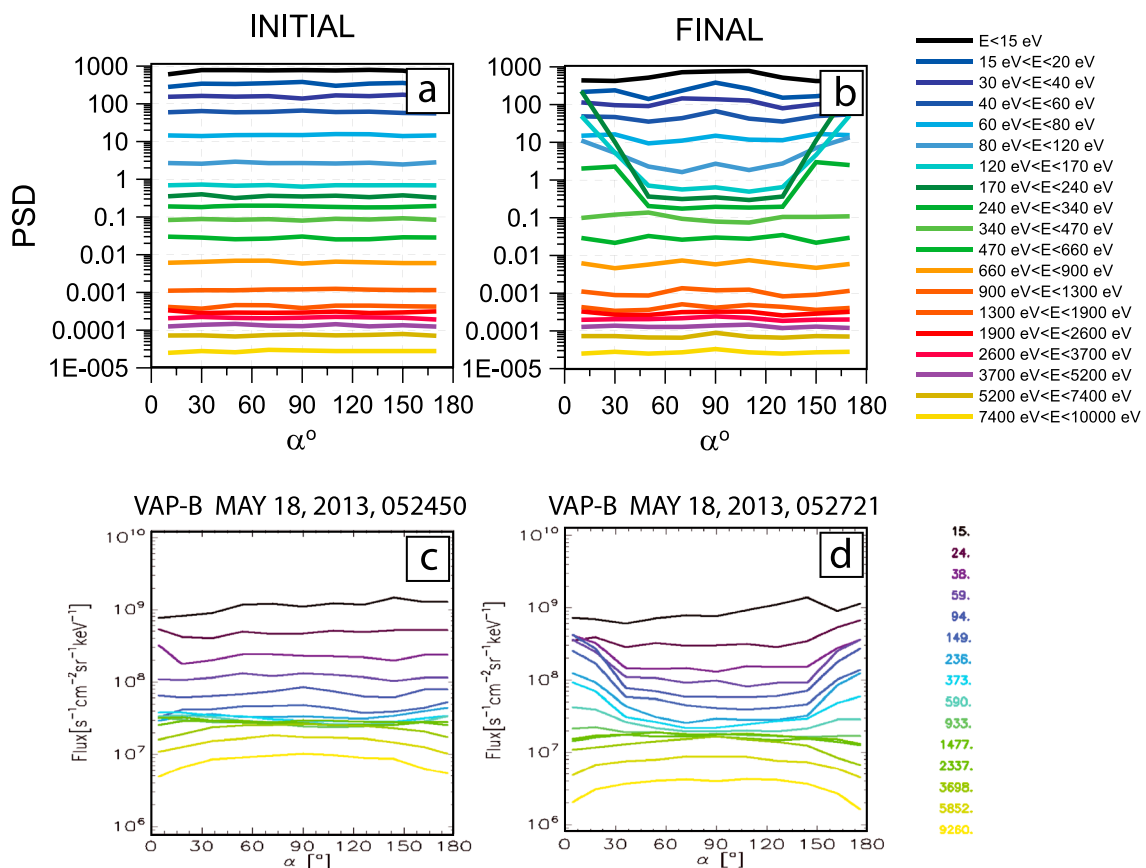


Figure 8. Comparison of Van Allen Probe data with a field-aligned electron pitch angle distribution produced in a simulation of electron interactions with 20 mV/m packets of electrostatic, TDS.

current system that produced dipolarization of the magnetic field. Approximately 10 such cases have been studied in detail, and the initial pitch angle distributions of the injected electrons in all cases were isotropic or peaked at 90°. In all cases, field-aligned pitch angle distributions and TDS appeared a few minutes following the injections and, in the majority (but not all) of the cases, these distributions and TDS occurred at the time of currents, as observed by the changing background magnetic field.

Because the field-aligned electron distributions of Figures 2 and 3 are very different from each other and because several different types of TDS exist (Figure 1), it is important to consider which types of TDS produce which types of accelerated electron pitch angle distributions and to understand the mechanisms for such production. It has been shown that field-aligned electron pitch angle distributions to energies of several keV can be produced by Landau interaction in a single electrostatic TDS having no net potential [Artemyev *et al.*, 2014b; Osmane and Pulkkinen, 2014]. A second mechanism involves electron interactions with many electrostatic TDS, as illustrated in Figure 8, in which Figures 8a and 8b present the before and after pitch angle distributions in a test particle simulation and Figures 8c and 8d illustrate before and after observations in space during an event involving electrostatic TDS of the type shown in Figure 1 (bottom left) and assumed in the simulation. In both the simulation and the space data, electrons with energies of 50–500 eV become field aligned while both lower energy and higher-energy electrons were relatively unaffected. Particle trajectories in the simulation show that electrons were accelerated parallel to the magnetic field by reflection from the TDS when the electron and TDS phase velocities were similar. Electron scattering by the perpendicular electric field in the TDS was not considered. In the simulation, TDS were generated near the equator at $L = 6$ in packets of typically 50 individual TDS having a maximum amplitude of 20 mV/m and a velocity of 4000 km/s. They propagated in a dipole magnetic field to a latitude of 40° where they were lost and a new packet was created at the equator. The initial particle distribution was the sum of three isotropic Maxwellians with temperatures of 10, 100, and 2000 eV and

with the hotter densities being 0.025 and 0.001 of the cold density. The simulation lasted about one bounce period of the cold electrons, during which about eight packets of TDS were generated. About 135,000 particles were included in the simulation. It produced field alignment such that the flux at 0 or 180° is several orders-of-magnitude larger than the flux at 90° (Figure 8). In the space data, this flux enhancement is something less than a factor of 10. Similar pitch angle distributions are seen early in Figures 2f and 3 (except that reflecting electrons are lost in this case).

In Figure 2 and in the event described in Figure 4, the pitch angle distributions became field aligned to energies as great as 100 keV (the Figure 4 pitch angle distributions are not shown). Looking across the four pitch angle distribution panels in Figure 2, it is seen that electrons below about 100 eV did not become field aligned and their fluxes were roughly constant with time. At any higher energy, the omnidirectional flux varied little during the time interval of interest, as can be seen in Figure 2c where the omnidirectional fluxes from 0514 to 0516 UT varied by less than a factor of 2. Thus, the parallel electrons at any energy in Figure 2g likely came largely from the deficit of 90° electrons. The parallel electric field in TDS cannot produce this result because the first invariant of the electron motion is conserved in the presence of only a parallel field. However, the perpendicular electric field in three-dimensional TDS, such as those in Figure 1, can cause the first invariant to become nonconserved if the electron crosses the TDS in a time that is short or comparable to its gyroperiod. In this case the electron energy can be redistributed between the perpendicular and parallel components and original 90° electrons might become field-aligned. Preliminary estimates and simulations suggest that a process like this may be happening.

The TDS that produced the 100 keV field-aligned distribution in Figure 2 were the electromagnetic TDS illustrated in Figure 1 (top right). The same type of TDS was associated with the field-aligned distributions that produced the aurora of Figure 4. Thus, it seems likely that the electromagnetic nature of the TDS (spikes in the parallel magnetic field component) is important in making energetic field-aligned distributions because such spikes are associated with an induced electric field that is not included in simpler discussions.

In Figure 3, the 100 eV–1 keV, 150–180° pitch angle flux remained large for many electron bounce periods while an order-of-magnitude fewer electrons returned at pitch angles of 0–30°. Thus, the large pitch angle electrons must have been lost in one or a few bounce periods. This requires continuous acceleration of 150–180° electrons. This electron beam was moving tailward in a tail-like magnetic field that was within the GSE-XY plane to less than 5°.

The data set of 200 events was produced by selecting time intervals during which TDS were present in the absence of any other wave activity (other than low-frequency noise). Field-aligned electron pitch angle distributions were present, at least part of the time, in every event in this data set. An alternative approach is to form a data set from events having field-aligned distributions and to inquire about TDS and other waves that are present at such times. In this data set, TDS were present in a clear majority of the cases and at least half of these cases had only TDS. These statistics suggest that TDS are often responsible for producing the field-aligned, accelerated electrons that are the seed population for relativistic acceleration and for precipitation that makes auroras. Thus, inclusion of TDS in radiation belt and auroral dynamics and theories seems to be required.

Acknowledgments

The data used in this paper are available at the Van Allen Probe Web site, <http://rbspgway.jhuapl.edu/>. The authors thank the scientists and engineers associated with the EFW, EMFISIS, MagEIS, and HOPE instruments for providing the high-quality data reported in this paper. The work by O.A., S.L., and F.M. was performed under JHU/APL contract 922613 (RBSP-EFW). The work of V.K. was partially supported by MK-1781.2014.2. The work of I.V. and A.A. was supported by presidential grant MK-1781.2014.2.

The Editor thanks Adnane Osmane and an anonymous reviewer for their assistance in evaluating this paper.

References

- Abel, G. A., A. N. Fazakerley, and A. D. Johnstone (2002a), Statistical distributions of field-aligned electron events in the near-equatorial magnetosphere observed by the Low Energy Plasma Analyzer on CREEPS, *J. Geophys. Res.*, 107(A11), 1393, doi:10.1029/2001JA005073.
- Abel, G. A., A. N. Fazakerley, and A. D. Johnstone (2002b), Simultaneous acceleration and pitch angle scattering of field-aligned electrons observed by the LEPA on CREEPS, *J. Geophys. Res.*, 107(A12), 1416, doi:10.1029/2001JA005090.
- Agapitov, O. V., A. Artemyev, D. Mourenas, V. Krasnoselskikh, J. Bonnell, O. Le Contel, C. M. Cully, and V. Angelopoulos (2014), The quasi-electrostatic mode of chorus waves and electron nonlinear acceleration, *J. Geophys. Res. Space Physics*, 119, 1606–1626, doi:10.1002/2013JA019223.
- Alfvén, H., and P. Carlqvist (1978), Interstellar clouds and the formation of start, *Astrophys. Space Sci.*, 55(2), 487–509.
- Andersson, L., et al. (2009), New features of electron phase space holes observed by the THEMIS mission, *Phys. Rev. Lett.*, 102, 225004, doi:10.1103/PhysRevLett.102.225004.
- Artemyev, A. V. (2014), Fast transport of resonant electrons in phase space due to nonlinear trapping by whistler waves, *Geophys. Res. Lett.*, 41, 5727–5733, doi:10.1002/2014GL061380.
- Artemyev, A. V., V. V. Krasnoselskikh, O. V. Agapitov, D. Mourenas, and G. Rolland (2012), Non-diffusive resonant acceleration of electrons in the radiation belts, *Phys. Plasmas*, 19, doi:10.1063/1.4769726.

- Artemyev, A. V., A. A. Vasiliev, D. Mourenas, O. V. Agapitov, and V. V. Krasnoselskikh (2013), Nonlinear electron acceleration by oblique whistler waves: Landau resonance vs. cyclotron resonance, *Phys. Plasmas*, 21, doi:10.1063/1.4836595.
- Artemyev, A., O. V. Agapitov, F. S. Mozer, and V. Krasnoselskikh (2014a), Thermal electron acceleration by localized bursts of electric field in the radiation belts, *Geophys. Res. Lett.*, 41, 5734–5739, doi:10.1002/2014GL061248.
- Artemyev, A. V., A. A. Vasiliev, D. Mourenas, O. V. Agapitov, and V. V. Krasnoselskikh (2014b), Electron scattering and non-linear trapping by oblique whistler waves: The critical wave intensity for non-linear effects, *Phys. Plasmas*, 21, doi:10.1063/1.4897945.
- Bale, S. D., D. Burgess, P. J. Kellogg, K. Goetz, R. L. Howard, and S. J. Monson (1996), Phase coupling in Langmuir wave packets: Possible evidence of three-wave interactions in the upstream solar wind, *Geophys. Res. Lett.*, 23, 109–112, doi:10.1029/95GL03595.
- Bale, S. D., P. J. Kellogg, D. E. Larsen, R. P. Lin, K. Goetz, and R. P. Lepping (1998), Bipolar electrostatic structures in the shock transition region: Evidence of electron phase space holes, *Geophys. Res. Lett.*, 25, 2929–2932, doi:10.1029/98GL02111.
- Berthomier, M., R. Pottelette, and M. Malingre (1998), Solitary waves and weak double layers in a two-electron temperature auroral plasma, *J. Geophys. Res.*, 103, 4261–4270, doi:10.1029/97JA00338.
- Cattell, C., J. Crumley, J. Dombeck, J. Wygant, and F. S. Mozer (2002), Polar observations of solitary waves at the Earth's magnetopause, *Geophys. Res. Lett.*, 29, 9–1, doi:10.1029/2001GL014046.
- Cattell, C., C. Neiman, J. Dombeck, J. Crumley, J. Wygant, C. A. Kletzing, W. K. Peterson, F. S. Mozer, and M. Andre (2003), Large amplitude solitary waves in and near the Earth's magnetosphere, magnetopause and bow shock: Polar and Cluster observations, *Science*, 299, 383–6.
- Chaston, C. C., et al. (2014), Observations of kinetic scale field line resonances, *Geophys. Res. Lett.*, 41, 209–215, doi:10.1002/2013GL058507.
- Deng, X., M. Ashour-Abdalla, M. Zhou, R. Walker, M. El-Alaoui, V. Angelopoulos, R. E. Ergun, and D. Schriver (2010), Wave and particle characteristics of earthward electron injections associated with dipolarization fronts, *J. Geophys. Res.*, 115, A09225, doi:10.1029/2009JA015107.
- Donovan, E., et al. (2006), The THEMIS All-Sky Imager Array—System design and initial results from the prototype imager, *J. Atmos. Sol. Terr. Phys.*, doi:10.1016/j.jastp.2005.03.27.
- Drake, J. F., O. V. Agapitov, and F. S. Mozer (2015), Development of a bursty precipitation front with intense localized parallel electric fields driven by whistler waves in the Earth's outer radiation belt, *Geophys. Res. Lett.*, doi:10.1002/2015GL063528.
- Ergun, R. E., et al. (1998), FAST satellite observations of large-amplitude solitary structures, *Geophys. Res. Lett.*, 25, 2041–2044, doi:10.1029/98GL00636.
- Ergun, R. E., Y.-J. Su, L. Andersson, C. W. Carlson, J. P. McFadden, F. S. Mozer, D. L. Newman, M. V. Goldman, and R. J. Strangeway (2001), Direct observation of localized parallel electric fields in a space plasma, *Phys. Rev. Lett.*, 87(4), 045003, doi:10.1103/PhysRevLett.87.045003.
- Ergun, R. E., et al. (2009), Observations of double layers in Earth's plasma sheet, *Phys. Rev. Lett.*, 102(15), 155002, doi:10.1103/PhysRevLett.102.155002.
- Fox, W., M. Porkolab, J. Egedal, N. Katz, and A. Le (2008), Laboratory observation of electron phase-space holes during magnetic reconnection, *Phys. Rev. Lett.*, 101(25), 255003, doi:10.1103/PhysRevLett.101.255003.
- Franz, J. R., P. M. Kintner, and J. S. Pickett (1998), POLAR observations of coherent electric field structures, *Geophys. Res. Lett.*, 25(8), 1277–1280, doi:10.1029/98GL50870.
- Goldman, M. V., M. M. Oppenheim, and D. L. Newman (1999), Nonlinear two-stream instabilities as an explanation for auroral bipolar wave structures, *Geophys. Res. Lett.*, 26(13), 1821–1824, doi:10.1029/1999GL900435.
- Hubbard, R. F., and G. Joyce (1979), Simulation of auroral double layers, *J. Geophys. Res.*, 84, 4297–4303, doi:10.1029/JA084iA08p04297.
- Joyce, G., and R. F. Hubbard (1978), Numerical simulation of plasma double layers, *J. Plasma Phys.*, 2391.
- Karpman, V. I., and R. N. Kaufman (1982), Self-focusing of whistlers, *Zh. Eksp. Teor. Fiz.*, 83.
- Kellogg, P. J., C. A. Cattell, K. Goetz, S. J. Monson, and L. B. Wilson III (2010), Electron trapping and charge transport by large amplitude whistlers, *Geophys. Res. Lett.*, 37, L20106, doi:10.1029/2010GL044845.
- Khotyaintsev, Y. V., A. Vaivads, M. Andre, M. Fujimoto, A. Retino, and C. J. Owen (2010), Observations of slow electron holes at a magnetic reconnection site, *Phys. Rev. Lett.*, 105(16), 165002, doi:10.1103/PhysRevLett.105.165002.
- Kletzing, C. A., et al. (2013), The Electric and Magnetic Field Instrument Suite and Integrated Science (EMFISIS) on RBSP, *Space Sci. Rev.*, 179, 127–181, doi:10.1007/s11214-013-9993-6.
- Lakhina, G. S., D. A. Gurnett, N. Cornilleau-Wehrlin, A. N. Fazakerley, I. Dandouras, and E. Lucek (2010), On the propagation and modulation of electrostatic solitary waves observed near the magnetopause on Cluster, *Modern Challenges in Nonlinear Plasma Physics: A Festchrift Honoring the Career of K Papadopoulos*, AIP Conference Proceedings 1320, American Institute of Physics, Melville, N. Y.
- Lashmore-Davies, C., and T. Martin (1973), Electrostatic instabilities driven by an electric current perpendicular to a magnetic field, *Nucl. Fusion*, 13(2), 193.
- Lefebvre, B., L.-J. Chen, W. Gekelman, P. Kintner, J. Pickett, P. Pribyl, and S. Vincena (2011), Debye-scale solitary structures measured in a beam-plasma laboratory experiment, *Nonlinear Processes Geophys.*, 18(1), 41–47, doi:10.5194/npg-18-41-2011.
- Li, S. Y., Y. Omura, B. Lembège, X. H. Deng, H. Kojima, Y. Saito, and S. F. Zhang (2014), Geotail observations of counter directed ESWs associated with the separatrix of magnetic reconnection in the near-Earth magnetotail, *J. Geophys. Res. Space Physics*, 119, 202–210, doi:10.1002/2013JA018920.
- Malaspina, D. M., D. L. Newman, L. B. I. I. Wilson, K. Goetz, P. J. Kellogg, and K. Kersten (2013), Electrostatic solitary waves in the solar wind: Evidence for instability at solar wind current sheets, *J. Geophys. Res. Space Physics*, 118, 591–599, doi:10.1002/jgra.50102.
- Malaspina, D. M., L. Andersson, R. E. Ergun, J. R. Wygant, J. W. Bonnell, C. Kletzing, G. D. Reeves, R. M. Skoug, and B. A. Larsen (2014), Nonlinear electric field structures in the inner magnetosphere, *Geophys. Res. Lett.*, 41, 5693–5701, doi:10.1002/2014GL061109.
- Matsumoto, H., H. Kojima, T. Miyatake, Y. Omura, M. Okada, I. Nagano, and M. Tsutsui (1994), Electrotastic Solitary Waves (ESW) in the magnetotail: BEN wave forms observed by GEOTAIL, *Geophys. Res. Lett.*, 21, 2915–2918, doi:10.1029/94GL01284.
- Mende, S. B., et al. (2008), The THEMIS array of ground-based observatories for the study of auroral substorms, *Space Sci. Rev.*, 141, 357–387, doi:10.1007/s11214-008-9380-x.
- Miyake, T., Y. Omura, H. Matsumoto, and H. Kojima (1998), Two-dimensional computer simulations of electrostatic solitary waves observed by Geotail spacecraft, *J. Geophys. Res.*, 103(A6), 11,841–11,850, doi:10.1029/98JA00760.
- Morse, R. L., and C. W. Nielson (1969a), Numerical simulation of warm two-beam plasma, *Phys. Fluids*, 12(11), 2418–2425.
- Morse, R. L., and C. W. Nielson (1969b), One-, two-, and three-dimensional numerical simulation of two-beam plasmas, *Phys. Rev. Lett.*, 23, 1087–1090.
- Mozer, F. S., and P. L. Pritchett (2009a), Regions associated with electron physics in asymmetric magnetic field reconnection, *Geophys. Res. Lett.*, 36, L07102, doi:10.1029/2009GL037463.
- Mozer, F. S., and P. L. Pritchett (2009b), The spatial, temporal, and amplitude characteristics of parallel electric fields associated with sub-solar magnetic field reconnection, *J. Geophys. Res.*, A04220, doi:10.1029/2009JA014718.

- Mozer, F. S., C. W. Carlson, M. K. Hudson, R. B. Torbert, B. Parady, J. Yattea, and M. C. Kelley (1977), Observations of paired electrostatic shocks in the polar magnetosphere, *Phys. Rev. Lett.*, 38, 292–295, doi:10.1103/PhysRevLett.38.292.
- Mozer, F. S., S. D. Bale, J. W. Bonnell, C. C. Chaston, I. Roth, and J. Wygant (2013), Megavolt parallel potentials arising from double-layer streams in the Earth's outer radiation belt, *Phys. Rev. Lett.*, 111(23), 235002, doi:10.1103/PhysRevLett.111.235002.
- Mozer, F. S., O. V. Agapitov, V. Krasnoselskikh, S. Lejosne, G.-D. Reeves, and I. Roth (2014), Direct observation of radiation-belt electron acceleration from electron-volt energies to megavolts by nonlinear whistlers, *Phys. Rev. Lett.*, 113, 035001, doi:10.1103/PhysRevLett.113.035001.
- Newman, D. L., M. V. Goldman, R. E. Ergun, and A. Mangeney (2001), Formation of double layers and electron holes in a current driven space plasma, *Phys. Rev. Lett.*, 87(25), 255001, doi:10.1103/PhysRevLett.87.255001.
- Omura, Y., H. Matsumoto, T. Miyake, and H. Kojima (1996), Electron beam instabilities as generation mechanism of electrostatic solitary waves in the magnetotail, *J. Geophys. Res.*, 101(A2), 2685–2697, doi:10.1029/95JA03145.
- Omura, Y., Y. Katoh, and D. Summers (2008), Theory and simulation of the generation of whistler-mode chorus, *J. Geophys. Res.*, 113, A04223, doi:10.1029/2007JA012622.
- Oppenheim, M. M., G. Vettouli, D. L. Newman, and M. V. Goldman (2001), Evolution of electron phase-space holes in 3D, *Geophys. Res. Lett.*, 28, 1891–1893, doi:10.1029/2000GL012383.
- Osmane, A., and A. M. Hamza (2012a), Relativistic particle acceleration as a consequence of Hopf bifurcation with application to the radiation belt electrons, *Phys. Plasmas*, 19, doi:10.1063/1.3692234.
- Osmane, A., and A. M. Hamza (2012b), Dynamical systems approach to relativistic nonlinear wave-particle interaction in collisionless plasmas, *Phys. Rev.*, 85, doi:10.1103/PhysRevE.85.056410.
- Osmane, A., and T. I. Pulkkinen (2014), On the threshold energization of radiation belt electrons by double layers, *J. Geophys. Res. Space Physics*, 119, 8243–8248, doi:10.1002/2014JA020236.
- Raadu, M. A. (1989), The physics of double layers and their role in astrophysics, *Phys. Rep.*, 178, 25–97.
- Roberts, K. V., and H. L. Berk (1967), Nonlinear evolution of a two-stream instability, *Phys. Rev. Lett.*, 19, 297–300.
- Roth, I., M. Temerin, and M. K. Hudson (1999), Resonant enhancement of relativistic electron fluxes during geomagnetically active periods, *Ann. Geophys.*, 17, 631–638.
- Saeki, K., P. Michelsen, H. L. Pécseli, and J. J. Rasmussen (1979), Formation and coalescence of electron solitary holes, *Phys. Rev. Lett.*, 42, 501–504.
- Shapiro, V. D., and S. K. Ride (1994), Nonlinear effects involving whistler wave propagation in the magnetosphere, *J. Geophys. Res.*, 99(A9), 17,237–17,247, doi:10.1029/94JA00718.
- Singh, N. (2003), Dynamically evolving double layers and density depletions, *J. Geophys. Res.*, 108(A8), 1322, doi:10.1029/2002JA009815.
- Spence, H. E., et al. (2013), Science goals and overview of the Energetic Particle, Composition, and Thermal Plasma (ECT) suite on NASA's Radiation Belt Storm Probes (RBSP) Mission, *Space Sci. Rev.*, doi:10.1007/s11214-013-0007-5.
- Streed, T., C. Cattell, F. Mozer, S. Kokubun, and K. Tsuruda (2001), Spiky electric fields in the magnetotail, *J. Geophys. Res.*, 106, 6276–6289, doi:10.1029/2000JA900154.
- Tao, J. B., et al. (2011), A model of electromagnetic electron phase-space holes and its application, *J. Geophys. Res.*, 116, A11213, doi:10.1029/2010JA016054.
- Temerin, M. A., K. Cerny, W. Lotko, and F. S. Mozer (1982), Observations of double layers and solitary waves in the auroral plasma, *Phys. Rev. Lett.*, 48, 1175–1179.
- Tsyganenko, N. A. (1995), Modeling the Earth's magnetospheric magnetic-field confined within a realistic magnetopause, *J. Geophys. Res.*, 100(A4), 5599–5612, doi:10.1029/94JA03193.
- Vasko, I., O. V. Agapitov, F. S. Mozer, A. Artemyev, and D. Jovanovic (2015), Magnetic field depression within electron holes, *Geophys. Res. Lett.*, 2123–2129, doi:10.1002/2015GL063370.
- Williams, J. D., L.-J. Chen, W. S. Kurth, D. A. Gurnett, M. K. Dougherty, and A. M. Rymer (2005), Electrostatic solitary structures associated with the November 10, 2003 interplanetary shock at 8.7 AU, *Geophys. Res. Lett.*, 32, L17103, doi:10.1029/2005GL23079.
- Williams, J. D., L.-J. Chen, W. S. Kurth, and D. A. Gurnett (2006), Electrostatic solitary structures observed at Saturn, *Geophys. Res. Lett.*, 33, L06103, doi:10.1029/2005GL024532.
- Wu, M., Q. Lu, A. Du, J. Xie, and S. Wang (2011), The evolution of the magnetic structures in electron phase-space holes: Two-dimensional particle-in-cell simulations, *J. Geophys. Res.*, 116, A10208, doi:10.1029/2011JA016486.
- Wygant, J. R., et al. (2013), The electric field and waves instruments on the Radiation Belt Storm Probes Mission, *Space Sci. Rev.*, 179, 183–220, doi:10.1007/s11214-013-0013-7.
- Yamamoto, T., and J. R. Kan (1985), Double layer formation due to current injection, *Planet. Space Sci.*, 33, 853–861.